Observation of *C*-type orbital ordered phase and orbital flipping in $LaVO_3$

Pavitra N. Shanbhag,[1] Francois Fauth,[2] and A. Sundaresan[1,*]

[1]*School of Advanced Materials, and Chemistry and Physics of Materials Unit, Jawaharlal Nehru Centre for Advanced Scientific Research, Jakkur P.O., Bangalore 560064, India*

[2]*CELLS-ALBA Synchrotron, E-08290 Cerdanyola del Vallès, Barcelona, Spain*

(Received 18 January 2023; accepted 3 October 2023; published 25 October 2023)

The orthovanadate system RVO_3 (R = rare-earth and Y) is known to exhibit multiple orbital, magnetic, and structural transitions depending on the size of the rare-earth ions. $LaVO_3$ is reported to exhibit a *G*-type orbital ordered (*G*-OO) phase and magnetization reversal below the antiferromagnetic transition. From high angular-resolution synchrotron x-ray powder diffraction measurements, we report the observation of the *C*-OO phase, hitherto unknown in $LaVO_3$, and its coexistence with the *G*-OO phase below T^1_{OO} (∼135 and 125 K) in ambient-pressure (AP) and high-pressure (HP) synthesized $LaVO_3$, respectively. At $T^2_{OO} \sim 20$ K, HP-$LaVO_3$ shows an orbital flipping transition from *G*- to *C*-OO, which results in an increase of the *C*-OO phase fraction. At 6 K, the *C*-OO phase becomes predominant (∼61%) in HP-$LaVO_3$, whereas it is ∼41% in AP-$LaVO_3$. We suggest that the different magnetic structures associated with coexisting orbital ordered phases should be responsible for the magnetization reversal phenomenon in $LaVO_3$.

DOI: 10.1103/PhysRevB.108.134115

I. INTRODUCTION

Mott insulating perovskite RVO_3 systems exhibit exotic properties such as temperature-induced magnetization reversal [1], orbital ordering, and spin ordering due to the coupling of lattice, spin, and orbital degrees of freedom [2]. In these perovskites, the V^{3+} magnetic ions have a d^2 electronic configuration, where two electrons can occupy any two of the triply degenerate orbital states d_{xy}, d_{yz}, and d_{xz}. The d_{xy} orbital will always be occupied with one of the t_{2g} electrons, and the occupation of the second electron in either the d_{yz} or d_{xz} orbital will determine the type of orbital ordering (OO). RVO_3 perovskites exhibit two kinds of OO states. One is *G*-OO, where d_{yz} and d_{xz} orbitals are occupied alternatively in all three crystallographic directions. The other one is *C*-OO, where d_{yz} and d_{xz} orbitals are occupied alternatively in the *ab*-plane, and similar orbitals are occupied (either d_{yz} or d_{xz}) along the *c*-direction [2,3]. RVO_3 crystallizes in the orthorhombic $GdFeO_3$-type distorted (tilting of the corner-sharing octahedra around the *b*-axis and rotating them around the *c*-axis) perovskite structure with space group *Pnma* in an orbital disordered (OD) state at room temperature where the VO_6 octahedron appears nearly isotropic [4,5]. The *G*-type orbital ordered state manifests as a change in crystal symmetry from orthorhombic (*Pnma*) to monoclinic ($P112_1/a$) phase. On the other hand, the *C*-type orbital ordered state remains in orthorhombic symmetry but with a highly distorted VO_6 octahedron having short and long bonds that alternate along the [101] and [10$\bar{1}$] directions of the *ac*-plane due to Jahn-Teller distortion [6]. Such anisotropy in the VO_6 octahedron can be assessed using high angular-resolution synchrotron x-ray powder diffraction to unambiguously identify the *C*- and/or *G*-OO structures. As a result of strong spin-orbit interaction, the spin ordering occurring due to the superexchange interaction is determined by the existing orbital ordering in the system. According to the Goodenough-Kanamori-Anderson rules [7–9], *G*- and *C*-type orbital ordering favor *C*- and *G*-type antiferromagnetic (AFM) exchange spin configurations, respectively. Rare-earth ions of bigger ionic radii, i.e., R = La-Nd, show *G*-OO/*C*-AFM as their ground state, while R^{3+} ions of intermediate ionic radii, such as R = Sm-Tb,Y exhibit *G*-OO in $T_N < T < T^1_{OO}$ and for a $T < T_N$ partial phase transition to *C*-OO/*G*-AFM coexisting with the *G*-OO/*C*-AFM down to low temperature. Further, RVO_3 with smaller ionic radii like R = Dy-Lu show *G*-OO in $T_N < T < T^1_{OO}$, *G*-OO/*C*-AFM in $T_N < T < T^2_{OO}$, and *C*-OO/*G*-AFM in $T < T^2_{OO}$ without any coexistence of orbital ordered phases [4,6,10]. Low-temperature neutron diffraction studies on RVO_3 (R = rare-earth and Y) except La evidenced the occurrence of orbital ordering before the spin ordering [2,5]. Such differences in the orbital/spin ordered states in these orthovanadates arise due to the different level of VO_6 octahedral tilting in the distorted perovskite. Octahedral tilting can be varied using external stimuli such as temperature, hydrostatic pressure [11], and magnetic field [12] to switch the orbital states.

The most exciting finding, which has attracted a lot of attention to the family of orthovanadates, is the observation of the temperature-induced magnetization reversal phenomenon. Goodenough *et al.* [13] observed this phenomenon for the first time in polycrystalline O′-orthorhombic $LaVO_3$ but not in other polycrystalline RVO_3 (R = Y,Lu). They proposed a mechanism of enhancement in the orbital angular moment upon cooling $LaVO_3$ through magnetostrictive transition at T_o, and this reverses the Dzyaloshinskii-Moriya vector to give a weak ferromagnetic spin moment opposite to the applied magnetic field below T_o. Later, magnetization reversal was

*Corresponding author: sundaresan@jncasr.ac.in

observed in single-crystal YVO_3 without any occurrence of structural change at T_o [14]. Ren *et al.* proposed a mechanism based on the competition between single-ion magnetic anisotropy and Dzyaloshinskii-Moriya interaction to give negative magnetization [15]. Questioning the assumptions of this model, Kimishima *et al.* proposed a theory based on *N*-type ferrimagnetism, which was used to explain the magnetization reversal in polycrystalline $SmVO_3$ and $NdVO_3$ [16,17]. Recent reports on YVO_3 presented the correlation of the phase coexistence of orbital/magnetic states with the magnetization reversal [10,18]. Further, to investigate the role of phase coexistence in other orthovanadates, the study has been extended to RVO_3 with a bigger-sized nonmagnetic rare-earth ion, $LaVO_3$. Though Raman studies on $LaVO_3$ single crystals [19] have shown the signatures of phase coexistence down to low temperatures, no detailed structural investigations have been reported.

On the other hand, O-orthorhombic $LaVO_3$ prepared by cold pressing the ambient pressure phase under a high pressure of $P \geqslant 8$ kbar was reported to show no sign of negative magnetization at low temperature [13]. Keeping this in mind, in the present study a detailed structural investigation of the orbital states is carried out on $LaVO_3$ prepared in two different conditions as described in Sec. II. These compounds contain slightly different oxygen stoichiometry and microstructure, which results in a different kind of magnetization reversal. Further, we observe the coexistence of *C*- and *G*-OO below T^1_{OO} in both compounds. Also, the OD O′-type orthorhombic unit cell transforms to the *G*-OO monoclinic phase coexisting with the *C*-OO O-type orthorhombic phase below T^1_{OO}. Additionally, an orbital flipping transition is observed below T^2_{OO}, where the *C*-OO O′-type orthorhombic phase grows at the expense of the *G*-OO monoclinic phase down to low temperature. Hence, we show that the phase coexistence of OO states is not just limited to RVO_3 of intermediate ionic radii (R = Sm-Tb,Y) but extends to *R* ions with bigger ionic sizes and is directly related to the observed temperature-dependent magnetization reversal phenomenon in orthovanadates.

II. EXPERIMENT

Polycrystalline samples of $LaVO_3$ were synthesized in two different ways: (i) solid-state reaction at high temperature under a hydrogen atmosphere, and (ii) high-pressure high-temperature synthesis. In the first method, $LaVO_3$ was synthesized by reducing the $LaVO_4$ under a pure H_2 (99.99%) atmosphere at 950 °C for 36 h with several intermittent grindings to improve the homogeneity of the sample. The polycrystalline powder of $LaVO_4$ was prepared by solid-state reaction using preheated La_2O_3 (Alfa Aesar, 99.99%) and V_2O_5 (Sigma Aldrich, 99.99%) in a 1:1 stoichiometric ratio, which were ground together and heated in air at 1000 and 1200 °C for 12 h with intermediate grinding. The prepared sample is therefore termed AP-$LaVO_3$. In the second method, AP-$LaVO_3$ was used as a starting material, and synthesis was carried out in a cubic-anvil high-pressure synthesis apparatus [20]. The starting material was encapsulated in a gold capsule, kept in a closed container made of a NaCl sleeve, and graphite was used as a heater. The sample was subjected to a pressure of ∼4.5 GPa and heated to a temperature of 950 °C. This reaction was maintained for 1 h, and the sample was recovered by quenching. Hence the obtained sample is termed HP-$LaVO_3$.

The phase purity of the as-synthesized powder sample was confirmed in the PANalytical Empyrean diffractometer using monochromatic Cu $K\alpha 1$ ($\lambda = 1.5406$ Å) by collecting room-temperature XRD data. Variable temperature synchrotron XRD data of $LaVO_3$ were collected during warming, with a wavelength 0.38692 Å on the material science powder diffraction beamline (BL04-MSPD) of the ALBA synchrotron facility (Barcelona area, Spain) using a Multi Analyzer Detection setup offering the highest angular resolution [21,22]. A liquid-helium Dynaflow cryostat was used to collect the XRD data at low temperatures [23]. Crystal structure analysis was done with the Rietveld refinement method using JANA2006 software. Temperature-dependent dc magnetization measurements were performed using a superconducting quantum interference device (SQUID) magnetometer (MPMS3) in the vibrating sample mode. Heat capacity was measured in the physical property measurement system (PPMS), Quantum Design, USA. X-ray photoelectron spectra (XPS) were recorded using a Thermo Scientific K Alpha spectrometer with a monochromatic Al $K\alpha$ radiation as the x-ray source. All the individual core-level spectra are corrected using the C 1*s* level signal (284.6 eV). The XPS measurements are carried out over pellet and thin-film samples. The thin film is obtained by drop casting a sample dispersed in isopropanol alcohol over silicon substrate. Before the measurement, first-layer (few nanometers) sample etching was done to remove any contamination over the surface. The obtained XPS spectra were fitted using a Shirley-type background function and an optimized combination of Lorentzian and Gaussian functions. Thermogravimetric analysis (TGA) was carried out using the Perkin-Elmer Pyris1 instrument. About 10 mg of the sample was loaded into a furnace using a platinum crucible and heated to the target temperature, 1000 °C, at a 5° C/ min rate.

III. RESULTS AND DISCUSSION

Figures 1(a) and 1(b) illustrate the zero field cooled (ZFC) and field cooled (FC) magnetization behavior of AP-$LaVO_3$ and HP-$LaVO_3$ measured with an applied field of 100 Oe, respectively. AP-$LaVO_3$ shows a magnetic anomaly at $T_N = 137$ K, below which the FC magnetization drops to give a negative magnetic moment down to low temperature, in agreement with the literature [13,24,25]. Such peculiar magnetization behavior is termed the temperature-induced magnetization reversal phenomenon.

On the other hand, HP-$LaVO_3$ shows a clear magnetic anomaly at $T_N = 127$ K but does not show negative magnetization even to the lowest magnetic field $H = 10$ Oe (see Fig. S1 in the Supplemental Material [26]). However, the FC susceptibility drops below the ZFC magnetization, indicating the tendency towards magnetization reversal. The absence of negative magnetization may be due to a paramagnetic contribution by the spins on V^{4+} sites that prevents the magnetic susceptibility curve from crossing the zero line below T_N in HP-$LaVO_3$. The presence of V^{4+} is confirmed by XPS analysis and is discussed later in detail. As shown in Fig. 1(b), the ZFC and FC curves of HP-$LaVO_3$ do not seem to coincide, and the reason behind this magnetization behavior is still

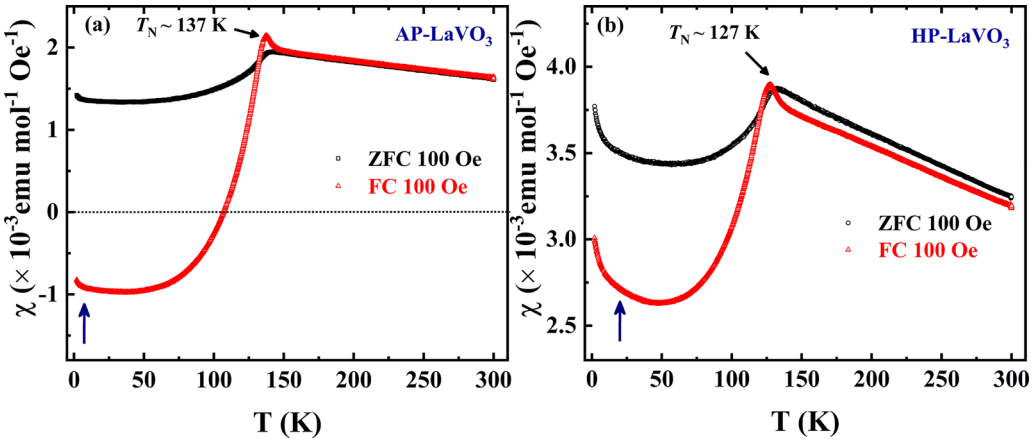

FIG. 1. DC magnetization measured at 100 Oe under zero field and field cooled conditions as a function of temperature for polycrystalline (a) AP-$LaVO_3$ and (b) HP-$LaVO_3$. The blue arrow at low temperature indicates the upturn in the magnetization.

unclear. Further, there is an upturn in the susceptibility curve below 50 K which is due to orbital flipping, as discussed later. The effective magnetic moment for both compounds is calculated by performing a Curie-Weiss fit in the paramagnetic region of temperature-dependent dc magnetization data, as shown in Fig. S2 of the Supplemental Material [26]. The obtained values of μ_{eff} are $3.46\mu_B$ and $3.97\mu_B$ for AP- and HP-$LaVO_3$, respectively. These values are higher than the spin-only magnetic moment for V^{3+}, i.e., $2.83\mu_B$. Earlier reports in the literature [27–29] obtained $\mu_{\text{eff}} \sim 3.8\mu_B$ for $LaVO_3$. Such an increase in the effective magnetic moment indicates a contribution from unquenched orbital angular momentum, suggesting the presence of spin-orbit coupling [30,31]. Other orthovanadates with a nonmagnetic rare earth, such as $LuVO_3$ and YVO_3, also show higher $\mu_{\text{eff}} \sim 3.3$ and $3.1\mu_B$, respectively [32,33]. From the thermogravimetric analysis, we have obtained the oxygen content of both ambient- and high-pressure samples, which is close to stoichiometric, ~3.095. Here, oxygen stoichiometry can play a significant role in determining the magnetic properties of $LaVO_3$. To carefully analyze the chemical difference and to obtain the oxidation state of the vanadium ions in both compounds, XPS spectra were recorded. Figures S3(a) and S3(b) of the Supplemental Material [26] show deconvoluted XPS core-level spectra obtained for AP-$LaVO_3$ and HP-$LaVO_3$, respectively. The XPS O 1*s* doublets in AP- and HP-$LaVO_3$ show peaks at a binding energy of ~531.5 and 529.8 eV, which corresponds to adsorbed oxygen (O_{ads}) and lattice oxygen (O_{latt}) at the surface, respectively [34]. The XPS signals corresponding to binding energies ~516 and ~522 eV derived from the fits are assigned as V $2p_{\frac{3}{2}}$ and V $2p_{\frac{1}{2}}$ of the V^{3+} state. Further, the deconvoluted peak observed at a binding energy ~525 eV is related to V $2p_{\frac{1}{2}}$ of the V^{4+} state [35]. The quantitative estimation of the elemental composition [36] was carried out using XPS peak areas and corresponding atomic sensitivity factors for AP and HP-$LaVO_3$, and it is shown in Table S1 of the Supplemental Material [26]. The obtained values of oxygen stoichiometry for AP and HP-$LaVO_3$ are ~3.14 and 3.26, respectively. This indicates that the HP-$LaVO_3$ have more V^{4+} compared to AP-$LaVO_3$ for charge compensation. To confirm this, the comparative spectral weight of V^{3+} and V^{4+} is obtained by quantifying the ratio of the integral area of the corresponding most intensive peaks. The relative spectral weight of the V^{4+}/V^{3+} ratio is 0.21 and 0.39 for AP- and HP-$LaVO_3$, respectively. The calculated molar ratio of $\frac{O_{\text{ads}}}{O_{\text{latt}}}$ for AP- and HP-$LaVO_3$ is 0.3 and 0.56, respectively.

To investigate the underlying mechanism behind the magnetization reversal in $LaVO_3$ and to explore the structural transitions across the low-temperature regime, temperature-dependent high-resolution synchrotron x-ray diffraction data were collected at several temperatures in the range 6–300 K. Rietveld refinement analysis on synchrotron XRD collected at room temperature confirms that the AP- and HP-$LaVO_3$ crystallize in $GdFeO_3$-type distorted orthorhombic perovskite structure with the *Pnma* space group, in agreement with earlier reports [37]. A careful analysis of the room-temperature XRD peak profile reveals broad peaks in the AP-$LaVO_3$ due to lattice strain caused by the reducing atmosphere used in the synthesis. In HP-$LaVO_3$, the peak broadening has significantly reduced, and the peak height has increased, as seen in the inset of Fig. S4 [26], indicating the reduction of lattice strain and a possible increase in crystallinity. The lattice strain of AP and HP-$LaVO_3$ is determined on synchrotron XRD data collected at 295 K using the Williamson-Hall equation [38],

$$\beta \cos\theta = \varepsilon(4\sin\theta) + \frac{K\lambda}{D},$$

where β is the integral breadth of the XRD reflection, D is the crystallite size, K is the shape factor (~0.9), λ is the wavelength of the x-ray used, ε is the lattice strain, and θ is Bragg's angle. The corresponding W-H plots of AP- and HP-$LaVO_3$ are shown in Fig. S5 [26]. The obtained lattice strain (ε) values for AP- and HP-$LaVO_3$ are $1.710(9)\times10^{-3}$ and $1.120(4)\times10^{-3}$, respectively. These values further support the idea that the lattice strain present in AP-$LaVO_3$ has reduced considerably in HP-$LaVO_3$. Such lattice strain manifested as peak broadening in the XRD peak shapes is also observed in Ga-doped V_2O_3 [39], prepared under a reducing atmosphere.

Upon cooling, AP-$LaVO_3$ changes the crystal symmetry from orthorhombic (*Pnma*) to monoclinic ($P112_1/a$) at $T_{OO}^1 =$ 135 K. This is evidenced by the splitting and broadening of the diffraction peaks (101) and (020), as shown in Fig. 2(a).

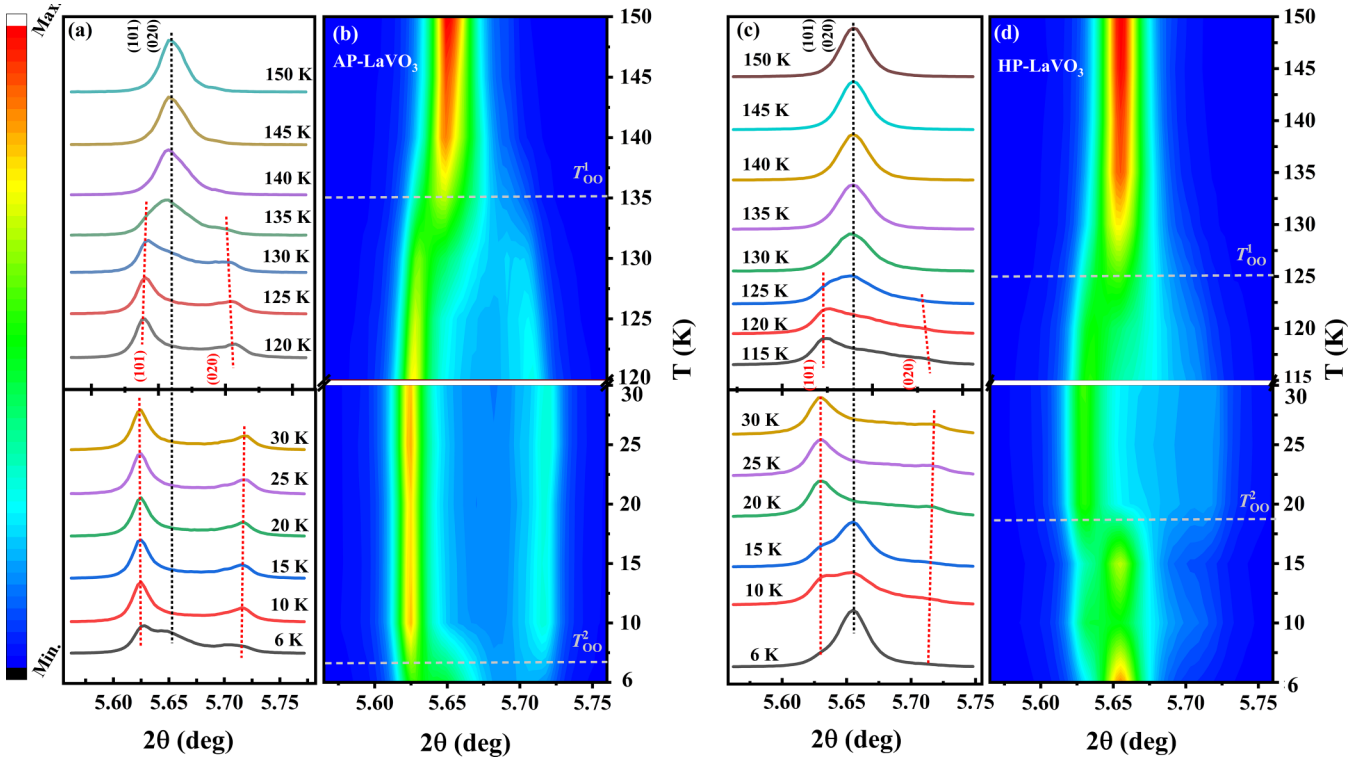

FIG. 2. Temperature-dependent synchrotron x-ray diffraction profiles with reflection (101) and (020) represented as (a),(c) a stack plot and (b),(d) a contour plot of AP-$LaVO_3$ and HP-$LaVO_3$, respectively. The black and red dotted lines indicate the evolution of reflections corresponding to orthorhombic and monoclinic phases, respectively, with temperature.

The black dotted line guides the eye to see the change in intensity of closely spaced diffraction reflections corresponding to the orthorhombic phase down to low temperature 6 K. The drastic change in the intensity of these reflections at 135 K can be clearly seen in the contour plot shown in Fig. 2(b). As the temperature reaches 135 K, new well-separated reflections (101) and (020) appear, indicating the change in the crystal symmetry to the monoclinic phase. The red dotted line guides the eye to track the evolution of diffraction lines (101) and (020) corresponding to the monoclinic phase down to low temperature. Cooling down the sample across 6 K, closely spaced reflections (101) and (020) reappear, indicating the growth of the orthorhombic phase. We observe similar results in HP-$LaVO_3$, except that it shows a symmetry change from the orthorhombic (*Pnma*) to the monoclinic ($P112_1/a$) phase at a slightly lower temperature, $T^1_{OO} = 125$ K, as shown in Figs. 2(c) and 2(d). At 15 K, the intensity of the reflections belonging to the orthorhombic phase starts to enhance, showing the growth of the orthorhombic phase, as observed in AP-$LaVO_3$.

Further, Rietveld refinement on synchrotron XRD collected at different temperatures was conducted to investigate the temperature-dependent structural evolution in both compounds. Rietveld refined synchrotron XRD profiles collected at 295, 100, and 6 K for AP-$LaVO_3$ and HP-$LaVO_3$ are shown in Figs. 3 and 4, respectively. The insets give a clear picture of the splitting and appearance of new reflections due to symmetry change. The refined structural parameters for AP- and HP-$LaVO_3$ are shown in Tables I and II, respectively. At room temperature, HP-$LaVO_3$ shows a compression

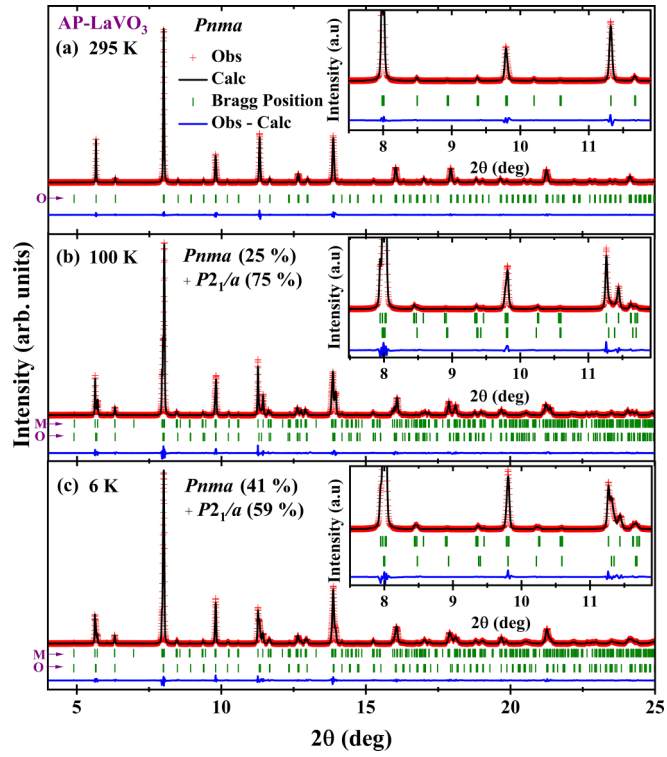

FIG. 3. Rietveld refined synchrotron x-ray diffraction profiles collected for AP-$LaVO_3$ at (a) 295 K, (b) 100 K, and (c) 6 K. *M* and *O* indicate Bragg planes corresponding to monoclinic and orthorhombic phases, respectively.

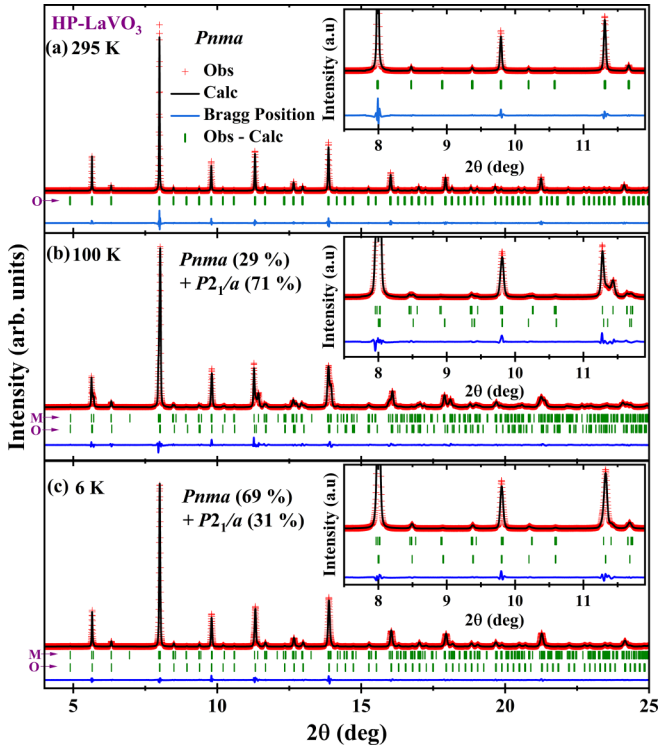

FIG. 4. Rietveld refined synchrotron x-ray diffraction profiles for HP-$LaVO_3$ collected at (a) 295 K, (b) 100 K, and (c) 6 K. *M* and *O* indicate Bragg planes corresponding to monoclinic and orthorhombic phases, respectively.

with a unit-cell contraction of $\Delta V \sim 0.25\%$ compared to AP-$LaVO_3$. At room temperature, the crystal structure consists of distorted VO_6 octahedra where lanthanum is situated between octahedral networks, as shown in Fig. 5(a). The distortion observed in these compounds corresponds to the $a^- b^+ a^-$ tilt system in Glazer notation [40]. Temperature-dependent unit-cell dimensions and the volume change for AP-$LaVO_3$ and HP-$LaVO_3$ are shown in Fig. 6.

We observe two significant anomalies in the unit-cell parameters. A high-temperature anomaly was observed at $T^1_{OO} \sim$ 135 and 125 K in AP- and HP-$LaVO_3$, respectively, indicating the structural transition from the orthorhombic (*Pnma*) to the monoclinic ($P2_1/a$) phase. This symmetry change is identified as an orbital ordering transition. In the orthorhombic phase, all the vanadium sites are equivalent. Due to symmetry lowering, two inequivalent vanadium sites appear to form alternate layers along the *b*-axis [5,37], as shown in Fig. 5(b).

In the orthorhombic phase, all the vanadium octahedra are tilted in three crystallographic axes and elongated along the [110] direction. As the symmetry changes to monoclinic, the elongation in the inequivalent vanadium octahedra increases, but 90° apart, and it occurs in all the crystallographic axes [5,37]. This kind of arrangement of VO_6 octahedra below T^1_{OO} is identified as *G*-type orbital ordering (*G*-OO) [5]. The monoclinic unit cell has elongated along the *a*- and *c*-axes and contracted along the *b*-axis, as seen in Figs. 6(a)–6(c) and Figs. 6(f)–6(h) for AP-$LaVO_3$ and HP-$LaVO_3$, respectively. The monoclinic unit cell angle for HP-$LaVO_3$ is around 89.89°–89.9° which seems to be slightly higher than that of AP-$LaVO_3$, i.e., approximately 89.86°–89.87° as shown in Figs. 6(i) and 6(d), respectively. These values are smaller but similar to that reported by Bordet et al., i.e., ∼90.125° [37], and Ren *et al.*, i.e., ∼90.10° [5], for $LaVO_3$ single crystals. The unit cell shows volume contraction across T^1_{OO} as the symmetry changes from orthorhombic to monoclinic phase, as seen in Figs. 6(e) and 6(j), respectively. Volume contraction (ΔV_M) of orthorhombic to monoclinic phase across T^1_{OO} is 0.015% and 0.055% for AP-$LaVO_3$ and HP-$LaVO_3$, respectively.

As the monoclinic phase grows below T^1_{OO}, the orthorhombic phase starts to reduce. Hence, there is a phase coexistence of orthorhombic and monoclinic phases observed below T^1_{OO}. This coexisting orthorhombic phase shows distinct behavior in ambient-pressure and high-pressure synthesized $LaVO_3$ below T^1_{OO}. In AP-$LaVO_3$, the coexisting orthorhombic unit cell contracts along the *b*-axis and elongates along the *a*- and *c*-axes, as seen in Figs. 6(a)–6(c). On the contrary, the coexisting orthorhombic unit cell of HP-$LaVO_3$ elongates along the *b*-direction, and contracts in the *a* and *c* directions, as shown in Figs. 6(f)–6(h). We observe a contraction in the orthorhombic unit cell volume below T^1_{OO} (ΔV_O) of 0.05% and 0.1% for ambient-pressure and high-pressure synthesized $LaVO_3$, as seen in Figs. 6(e) and 6(j), respectively. Upon further cooling, the signature of another phase transition is manifested as a sudden change in unit cell parameters and volume at $T^2_{OO} = 6$ and 20 K in AP-$LaVO_3$ and HP-$LaVO_3$, respectively. In the case of orthovanadates, the volume difference between orthorhombic and monoclinic unit cells (ΔV_{MO}) in the phase-separated region at 5 K is 0.07% in $SmVO_3$ [41], 0.12% in $EuVO_3$, 0.13% in $GdVO_3$, and 0.12% in $TbVO_3$ [4,6]. In the phase-separated region at 30 K, the ΔV_{MO} is 0.09% and 0.19% for AP-$LaVO_3$ and HP-$LaVO_3$, respectively. This difference in the unit-cell volume of the orthorhombic and monoclinic phases describes the degree of strain in the sample.

To investigate the nature of coexisting orthorhombic phases in $T^2_{OO} < T < T^1_{OO}$ and $T < T^2_{OO}$, the variation of $\frac{b}{\sqrt{2}c}$ is plotted as a function of temperature and is shown in Figs. 7(a) and 7(b). Both compounds show an O′-orthorhombic perovskite structure ($\frac{b}{\sqrt{2}c} < 1$) at room temperature. As the symmetry changes from orthorhombic to monoclinic, the ratio $\frac{b}{\sqrt{2}c}$ rapidly decreases. In AP-$LaVO_3$, the ratio $\frac{b}{\sqrt{2}c}$ for the coexisting orthorhombic phase reduces below T^1_{OO} and further increases below T^2_{OO}, but overall it remains less than 1. Surprisingly, the O′-orthorhombic phase in HP-$LaVO_3$ changes to the O-orthorhombic phase coexisting with the monoclinic phase below T^1_{OO}. Upon cooling down to T^2_{OO}, it again reverts to the O′-orthorhombic phase. All the polycrystalline rare-earth vanadates, RVO_3 (R = Ce, Pr, Nd, Sm, Eu, Gd, Tb, Y, and Lu), exist in the O-orthorhombic phase at room temperature except $LaVO_3$ [6]. Interestingly, the room-temperature structure of metastable $LaVO_3$ synthesized in high pressure ($P \geqslant 8$ kbar) was reported to show an O-orthorhombic perovskite ($\frac{b}{\sqrt{2}c} > 1$) which reverts to an O′-orthorhombic perovskite ($\frac{b}{\sqrt{2}c} < 1$) after heating it to 250 °C in hydrogen [13]. It seems that the application of physical or chemical pressure on RVO_3 perovskites can stabilize the O-orthorhombic phase.

TABLE I. Rietveld refined structural parameters for AP-$LaVO_3$ at different temperatures.

(a) ***T***=295 K; Space group - *Pnma* (Orthorhombic)

$a = 5.5504(1)$ Å, $b = 7.8512(2)$ Å, $c = 5.5549(1)$ Å and $\alpha = \beta = \gamma = 90^\circ$; V = 242.072(1) Å^3
Overall GoF = 2.23, $R_p = 5.13$ and $R_{wp} = 7.5\%$

Atomic coordinates	Occupancy	x	y	z	U_{iso} (Å^2)
La (4*c*)	1.0	0.02817(1)	0.25	0.9952(1)	0.0054(1)
V (4*b*)	1.0	0.5	0.0	0.0	0.0020(1)
O1 (4*c*)	1.0	0.4926(7)	0.25	0.0756(12)	0.0033(6)
O2 (8*d*)	1.0	0.2818(8)	0.0365(5)	0.7205(8)	0.0033(6)

(b) T=100 K; Overall GoF = 2.49, $R_p = 6.67$ and $R_{wp} = 9.27\%$
Phase I (24.99 %): Space group - *Pnma* (Orthorhombic)

$a = 5.5514(4)$ Å, $b = 7.8008(5)$ Å, $c = 5.5651(5)$ Å and $\alpha = \beta = \gamma = 90^\circ$; $R_p = 1.55$ and $R_{wp} = 2.39\%$

Atomic coordinates	Occupancy	x	y	z	U_{iso} (Å^2)
La (4*c*)	1.0	0.0368(3)	0.25	0.9928(5)	0.0016(1)
V (4*b*)	1.0	0.5	0.0	0.0	0.0002(1)
O1 (4*c*)	1.0	0.4848(24)	0.25	0.1018(36)	0.0005(4)
O2 (8*d*)	1.0	0.2834(25)	0.0580(14)	0.7163(27)	0.0005(4)

Phase II (75.01%): Space group − $P112_1/a$ (Monoclinic)

$a = 5.5863$ (1) Å, $b = 7.7621(1)$ Å, $c = 5.5634(1)$ Å and $\alpha = \beta = 90^\circ$, $\gamma = 89.870(1)^\circ$; $R_p = 2.55$ and $R_{wp} = 3.93\%$

Atomic coordinates	Occupancy	x	y	z	U_{iso} (Å^2)
La (4*e*)	1.0	0.0284(1)	0.25	0.9938(2)	0.0016(1)
V1 (2*c*)	1.0	0.5	0.0	0.0	0.0002(1)
V2 (2*d*)	1.0	0.0	0.5	0.5	0.0002(1)
O1 (4*e*)	1.0	0.4882(9)	0.25	0.0619(11)	0.0005(4)
O2 (4*e*)	1.0	0.2972(17)	0.0299(18)	0.7244(23)	0.0005(4)
O3 (8*e*)	1.0	0.7312(19)	0.5301(17)	0.2884(22)	0.0005(4)

(c) T=6 K; Overall GoF = 2.14, $R_p = 5.83$ and $R_{wp} = 7.98\%$
Phase I (41.07 %): Space group - *Pnma* (Orthorhombic)

$a = 5.5516$ (1) Å, $b = 7.8256(1)$ Å, $c = 5.5528(1)$ Å and $\alpha = \beta = 90^\circ$; $R_p = 2.66$ and $R_{wp} = 3.51\%$

Atomic coordinates	Occupancy	x	y	z	U_{iso} (Å^2)
La (4*c*)	1.0	0.0330(1)	0.25	0.9937(2)	0.0016(1)
V (4*b*)	1.0	0.5	0.0	0.0	0.0002(1)
O1 (4*c*)	1.0	0.4890(11)	0.25	0.0762(18)	0.0005(4)
O2 (8*d*)	1.0	0.2781(13)	0.0371(7)	0.7113(12)	0.0005(4)

Phase II (58.93%): Space group − $P112_1/a$ (Monoclinic)

$a = 5.5839$ (1) Å, $b = 7.7674(1)$ Å, $c = 5.5626(1)$ Å and $\alpha = \beta = 90^\circ$, $\gamma = 89.867(2)^\circ$; $R_p = 3.07$ and $R_{wp} = 3.89\%$

Atomic coordinates	Occupancy	x	y	z	U_{iso} (Å^2)
La (4*e*)	1.0	0.0290(1)	0.25	0.9944(1)	0.0021(1)
V1 (2*c*)	1.0	0.5	0.0	0.0	0.0002(1)
V2 (2*d*)	1.0	0.0	0.5	0.5	0.0002(1)
O1 (4*e*)	1.0	0.4888(8)	0.25	0.0695(10)	0.0005(4)
O2 (4*e*)	1.0	0.2977(17)	0.0406(17)	0.7302(22)	0.0005(4)
O3 (8*e*)	1.0	0.7222(19)	0.5359(17)	0.2875(22)	0.0005(4)

Further, the orthorhombic strain parameter is studied for ambient-pressure and high-pressure synthesized $LaVO_3$ as a function of temperature, and it is shown in Figs. 7(c) and 7(d), respectively. The orthorhombic strain parameter is defined as $s = \frac{2(a-c)}{(a+c)}$. This parameter is considered as a measure of octahedral distortion and is reported to increase with the octahedral tilting in RVO_3 perovskites [42]. The room-temperature orthorhombic strain in AP- and HP-$LaVO_3$ is

TABLE II. Rietveld refined structural parameters for HP-$LaVO_3$ at different temperatures.

(a) T=295 K; Space group - *Pnma* (Orthorhombic)

$a = 5.5391(1)$ Å, $b = 7.8453(2)$ Å, $c = 5.5564(6)$ Å and $\alpha = \beta = \gamma = 90^\circ$; V = 241.458(3) Å^3
Overall goodness of fit = 2.12, $R_p = 5.24$ and $R_{wp} = 8.11\%$

Atomic coordinates	Occupancy	x	y	z	U_{iso} (Å^2)
La (4*c*)	1.0	0.0291(4)	0.25	0.9947(2)	0.0034(1)
V (4*b*)	1.0	0.5	0.0	0.0	0.0013(1)
O1 (4*c*)	1.0	0.4915(5)	0.25	0.0681(10)	0.0027(5)
O2 (8*d*)	1.0	0.2842(6)	0.0387(5)	0.7162(7)	0.0027(5)

(b) T= 100 K; Overall GoF = 2.74, $R_p = 6.91$ and $R_{wp} = 9.88\%$
Phase I (29.01 %): Space group - *Pnma* (Orthorhombic)

$a = 5.5280(4)$ Å, $b = 7.8632(6)$ Å, $c = 5.5348(5)$ Å and $\alpha = \beta = \gamma = 90^\circ$; $R_p = 1.70$ and $R_{wp} = 2.87\%$

Atomic coordinates	Occupancy	x	y	z	U_{iso} (Å^2)
La (4*c*)	1.0	0.0383(2)	0.25	0.9949(6)	0.0032(1)
V (4*b*)	1.0	0.5	0.0	0.0	0.0007(2)
O1 (4*c*)	1.0	0.4931(22)	0.25	0.1340(41)	0.0005(2)
O2 (8*d*)	1.0	0.2834(26)	0.0435(20)	0.7091(24)	0.0005(2)

Phase II (70.99 %): Space group − $P112_1/a$ (Monoclinic)

$a = 5.5776(1)$ Å, $b = 7.7691(1)$ Å, $c = 5.5599$ (1) Å and $\alpha = \beta = 90^\circ$, $\gamma = 89.897(3)^\circ$; $R_p = 2.89$ and $R_{wp} = 4.40\%$

Atomic coordinates	Occupancy	x	y	z	U_{iso} (Å^2)
La (4*e*)	1.0	0.0246(1)	0.25	0.9946(2)	0.0032(1)
V1 (2*c*)	1.0	0.5	0.0	0.0	0.0007(2)
V2 (2*d*)	1.0	0.0	0.5	0.5	0.0007(2)
O1 (4*e*)	1.0	0.4831(11)	0.25	0.0627(14)	0.0005(2)
O2 (4*e*)	1.0	0.2982(23)	0.0285(30)	0.7249(35)	0.0005(2)
O3 (8*e*)	1.0	0.7442(28)	0.5279(29)	0.2841(30)	0.0005(2)

(c) T=6 K; Overall GoF = 2.32, $R_p = 4.89$ and $R_{wp} = 6.58\%$
Phase I (61.33 %): Space group - *Pnma* (Orthorhombic)

$a = 5.5400(1)$ Å, $b = 7.8457(2)$ Å, $c = 5.5489(1)$ Å and $\alpha = \beta = \gamma = 90^\circ$; $R_p = 2.20$ and $R_{wp} = 3.05\%$

Atomic coordinates	Occupancy	x	y	z	U_{iso} (Å^2)
La (4*c*)	1.0	0.0274(1)	0.25	0.9943(1)	0.0026(1)
V (4*b*)	1.0	0.5	0.0	0.0	0.0010(1)
O1 (4*c*)	1.0	0.4906(9)	0.25	0.0755(12)	0.0005(4)
O2 (8*d*)	1.0	0.2781(10)	0.0393(5)	0.7173(8)	0.0005(4)

Phase II (38.67 %): Space group − $P112_1/a$ (Monoclinic)
$a = 5.5521(2)$ Å, $b = 7.7885(3)$ Å, $c = 5.5693(2)$ Å and $\alpha = \beta = 90^\circ$, $\gamma = 89.923(5)^\circ$; $R_p = 2.06$ and $R_{wp} = 2.76\%$

Atomic coordinates	Occupancy	x	y	z	U_{iso} (Å^2)
La (4*e*)	1.0	0.0338(1)	0.25	0.9959(1)	0.0026(1)
V1 (2*c*)	1.0	0.5	0.0	0.0	0.0010(1)
V2 (2*d*)	1.0	0.0	0.5	0.5	0.0010(1)
O1 (4*e*)	1.0	0.4896(14)	0.25	0.0652(16)	0.0005(4)
O2 (4*e*)	1.0	0.2921(38)	0.0472(20)	0.7403(33)	0.0005(4)
O3 (8*e*)	1.0	0.7171(43)	0.5293(21)	0.2895(33)	0.0005(4)

~ -0.0008 and -0.0031, respectively. In AP-$LaVO_3$, below T_{OO}^1, the strain parameter decreases to -0.0017 at 100 K and gradually increases at lower temperatures. In HP-$LaVO_3$, the strain parameter drops at T_{OO}^1, but it increases and retains the same value until it reaches T_{OO}^2. Below T_{OO}^2, it becomes more negative and reaches $s \sim -0.0034$ at 6 K. It is evident in $YTiO_3$ perovskites that the orthorhombic strain increases with the application of pressure [43]. Observing the nature of the temperature dependence of the strain parameter, it seems that the orthorhombic unit-cell deformation of HP-$LaVO_3$ is

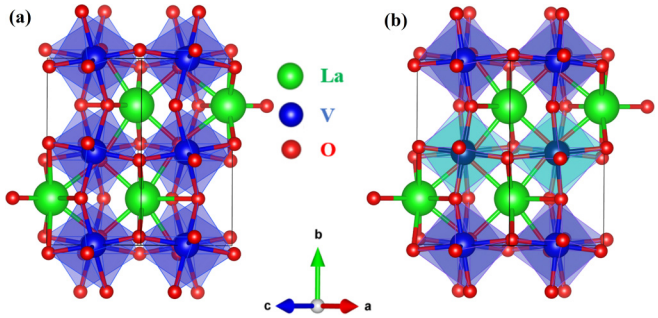

FIG. 5. Crystal structure of (a) the orthorhombic phase and (b) the monoclinic phase of $LaVO_3$. The monoclinic phase of $LaVO_3$ shows two inequivalent vanadium sites forming alternate VO_6 layers indicated by dark and light blue octahedra, whereas the orthorhombic phase shows a single vanadium site.

opposite to that of AP-$LaVO_3$ in the region $T_{OO}^2 < T < T_{OO}^1$ and $T < T_{OO}^2$. Indeed, the room-temperature orthorhombic phase of HP-$LaVO_3$ is deformed due to cooperative Jahn-Teller distortion and consequent octahedral tilting while cooling down to 6 K.

Further, to study the octahedral distortion across the structural phase transition and the corresponding orbital ordered states, the V-O_1 bond length along the *b*-axis and V-O_2 bond lengths in the *ac*-plane are plotted as a function of temperature for AP-$LaVO_3$ and HP-$LaVO_3$ as shown in Figs. 8(a) and 8(b), respectively. In the orthorhombic phase, the VO_6 octahedra consist of six V-O bonds of moderately similar length. Below T_{OO}^1, as the symmetry changes to the monoclinic phase, three pairs of V-O bonds appear where V-O_1 along the *b*-axis shows a slight decrease in the bond length, while

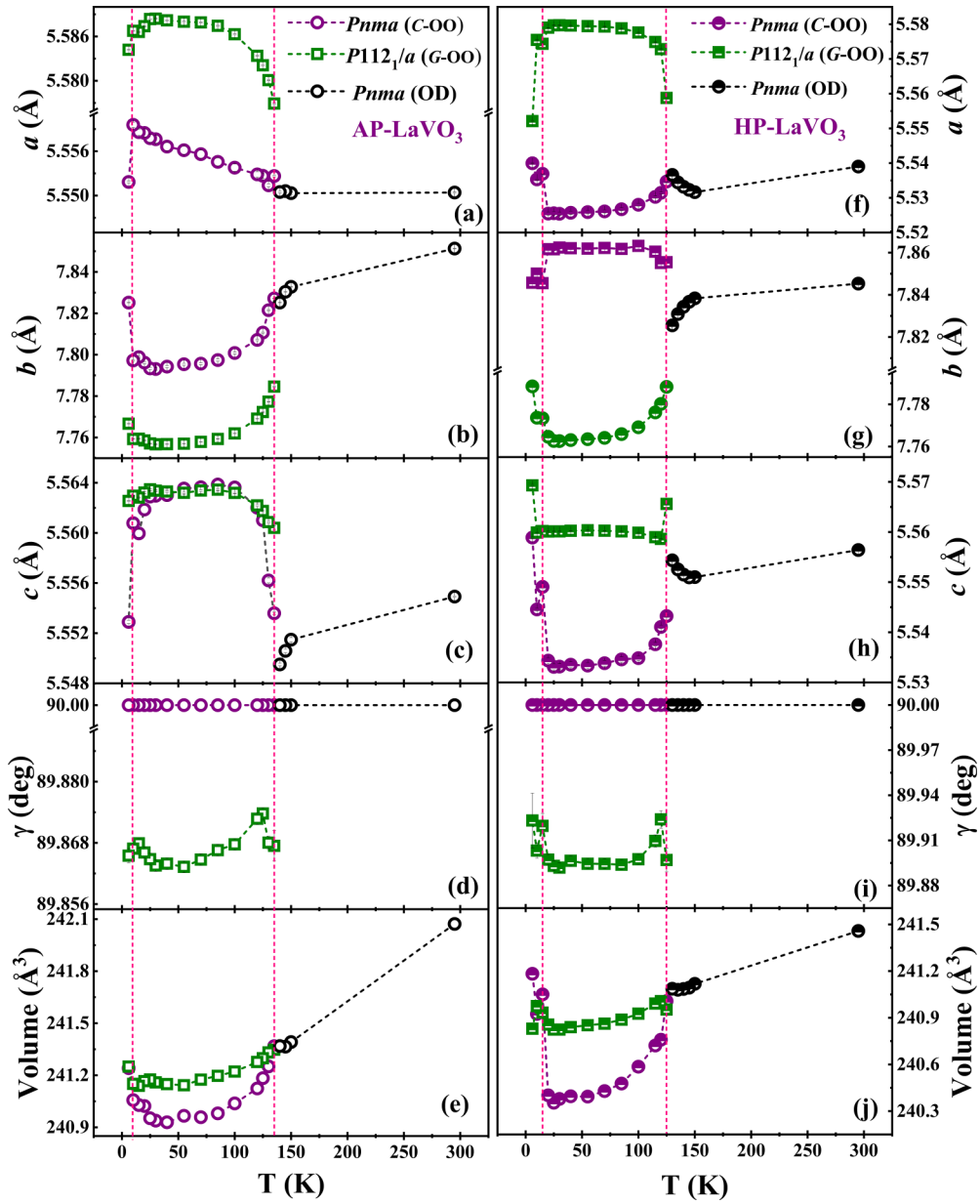

FIG. 6. Temperature dependence of (a)–(c),(f)–(h) cell parameters; (d),(i) monoclinic unit cell angle; and (e),(j) unit cell volume of orthorhombic and monoclinic phases for ambient-pressure and high-pressure $LaVO_3$. Error bars lie within the data symbols.

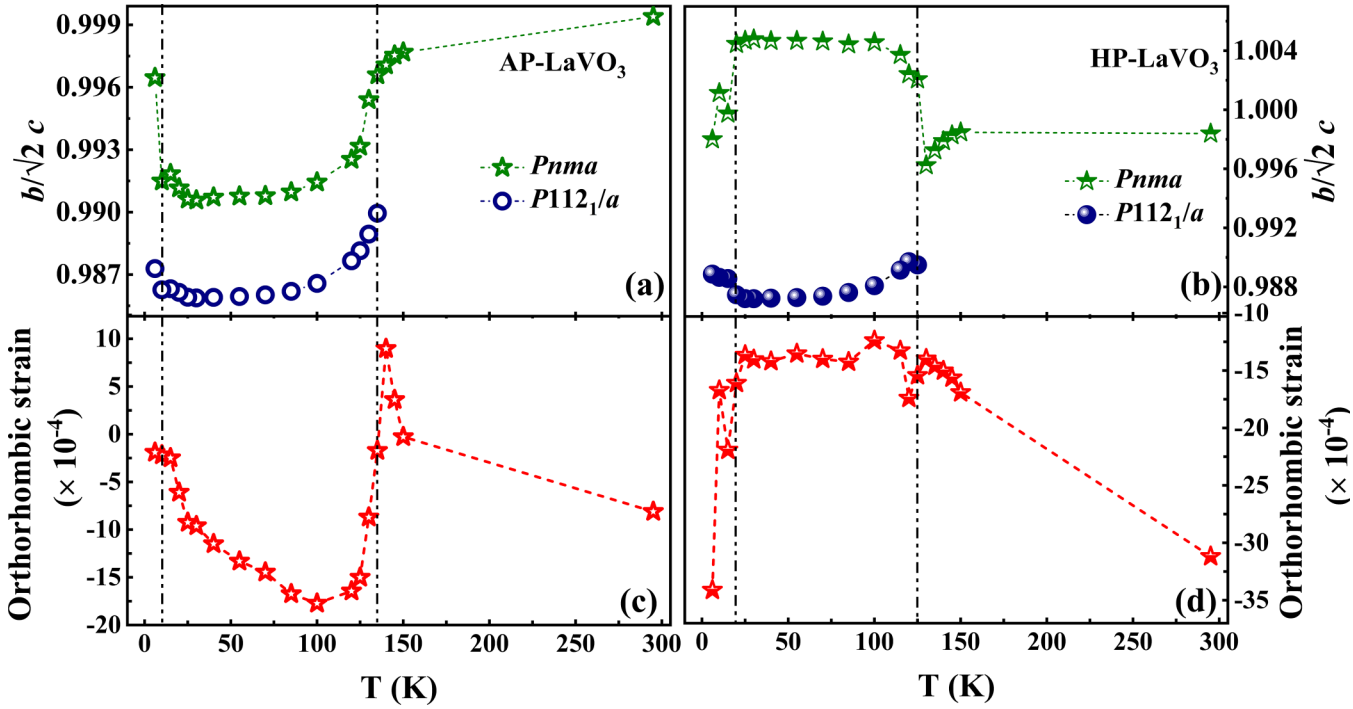

FIG. 7. Temperature dependence of (a),(b) $\frac{b}{\sqrt{2}c}$ ratio and (c),(d) strain in the orthorhombic unit cell for AP-$LaVO_3$ and HP-$LaVO_3$.

V-O_2 bond lengths change drastically in the *ac*-plane. One pair of the V-O_2 bond shortens while the other elongates in the equatorial *ac*-plane, indicating increased octahedral distortion in the monoclinic unit cell. Such a drastic change in the V-O bond lengths means the lifting of orbital degeneracy of the t_{2g} orbital of the V^{3+} (d^2) ion. Lowering the temperature below T^2_{OO}, we again observe a sudden jump in the V-O_1 and V-O_2 bond lengths, indicating the occurrence of another octahedral tilting. Changes in the V-O bond lengths below T^1_{OO} is reflected in the sudden change of the apical V-O_1-V bond angle, as seen in Figs. 8(c) and 8(d), respectively. As the distortion increases in the VO_6 octahedra, the apical V-O_1-V bond angle increases. Such octahedral distortion in the monoclinic unit cell brings selective occupation of electrons in the orbitals, which is called *G*-OO. In HP-$LaVO_3$, at T^2_{OO} the V-O_1-V bond angle drops suddenly, but upon further cooling it starts to increase, indicating relief from the octahedral distortion at T^2_{OO} followed by gradual octahedral tilting at lower temperatures.

The temperature-dependent evolution of the V-O bond distance in the orthorhombic phase is shown in Figs. 8(e) and 8(f), respectively. While cooling, we observe three pairs of distinctly different V-O bond distances below T^1_{OO} in AP and HP-$LaVO_3$. Here, the VO_6 octahedra of the orthorhombic unit cell distort drastically, which is manifested by the sudden elongation and compression of the V-O_2 bond distance in the *ac*-plane. Cooling down AP-$LaVO_3$ to low temperatures, the shorter V-O_2 bond elongates at 100 K, indicating relief from the octahedral distortion. Below T^2_{OO}, the V-O_2 bonds vary significantly to give increased octahedral distortion in the *ac*-plane. On the other hand, in HP-$LaVO_3$, the apical V-O_1 bond elongates, indicating octahedral elongation along the *b*-axis. Below T^2_{OO}, the V-O_1 bond contracts, and the difference in the V-O_2 bond length decreases, indicating reduced distortion in the *ac*-plane. Observing the V-O_2 bond lengths below T^1_{OO} [Figs. 8(e) and 8(f)], undoubtedly, the extent of octahedral distortion of the orthorhombic phase in AP-$LaVO_3$ is less than that of HP-$LaVO_3$. The distortion in the vanadium octahedra can be quantified by calculating the octahedral distortion parameter using the empirical formula, $\Delta d_V = \frac{1}{6}\sum_{i=1}^{6}\left(\frac{d_i - \langle d\rangle}{\langle d\rangle}\right)^2$, where $\langle d\rangle$ is the average V-O bond distance [44]. The room-temperature octahedral distortion parameter obtained for $LaVO_3$ is 8.960×10^{-6} and 9.482×10^{-6} for the ambient-pressure and high-pressure synthesized compound, respectively. These values are slightly lower than that reported in the literature [42]. Variation of VO_6 octahedral distortion with respect to temperature is shown in Figs. 8(g) and 8(h) for AP-$LaVO_3$ and HP-$LaVO_3$, respectively. The coexisting orthorhombic phase shows higher octahedral distortion in high-pressure synthesized $LaVO_3$ than in the ambient pressure sample. For the comparative study of octahedral distortion of the coexisting orthorhombic phase, the tilting angle is obtained using the expression $\Phi = \frac{180 - \langle \text{V-O-V}\rangle}{2}$, where $\langle$V-O-V$\rangle$ is the average bond angle between two VO_6 octahedra. While cooling across T^1_{OO}, we observe a drastic change in the tilting angle of the coexisting orthorhombic phase in ambient-pressure and high-pressure synthesized $LaVO_3$ as seen in Figs. 8(i) and 8(j), respectively. This is also manifested as a sudden change in the octahedral distortion parameter of the coexisting orthorhombic phase below T^1_{OO} in Figs. 8(g) and 8(h), respectively. All of these observations point toward the orbital ordering in the coexisting orthorhombic phase below T^1_{OO}. Such orbital ordering in the orthorhombic phase is identified as *C*-OO.

To systematically study the coexistence of *G*- and *C*-type orbital ordered states in AP-$LaVO_3$ and HP-$LaVO_3$, orthorhombic and monoclinic phase fractions are plotted as

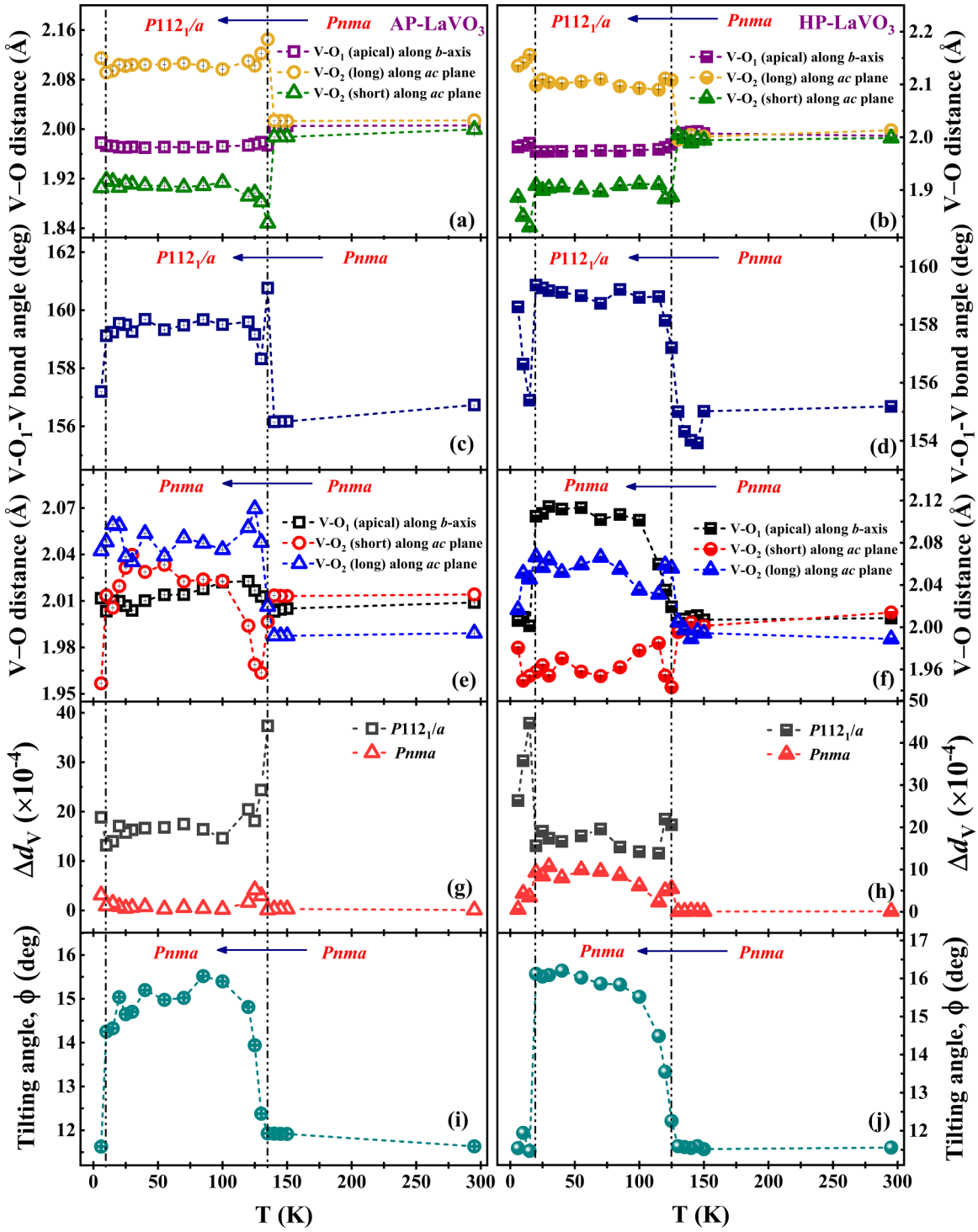

FIG. 8. Temperature dependence of (a),(b) V-O bond distance; (c),(d) V-O$_1$-V bond angle in VO_6 octahedra for orthorhombic to monoclinic transition; (e),(f) V-O bond distance in VO_6 octahedra of orthorhombic phase; (g),(h) octahedral distortion parameter calculated for orthorhombic and monoclinic phases; and (i),(j) tilting angle calculated for VO_6 octahedra in orthorhombic phase for ambient-pressure and the high-pressure sample of $LaVO_3$. Error bars lie within the data symbols.

a function of temperature and are shown in Figs. 9(a) and 9(b), respectively. There exist three different orbital states in $LaVO_3$, i.e., (i) the OD state (*Pnma*), (ii) the *C*-OO state (*Pnma*), and (iii) the *G*-OO state ($P2_1/a$). Both AP- and HP-$LaVO_3$ compounds exhibit all these orbital states at different temperature ranges, as shown in Fig. 9. In the temperature range $T > T_{OO}^1$, the OD orthorhombic phase exists, whereas in the region $T < T_{OO}^1$, the *G*- and *C*-OO phases coexist. In this temperature region, we observe the magnetization reversal phenomenon, and upon further cooling the sample toward

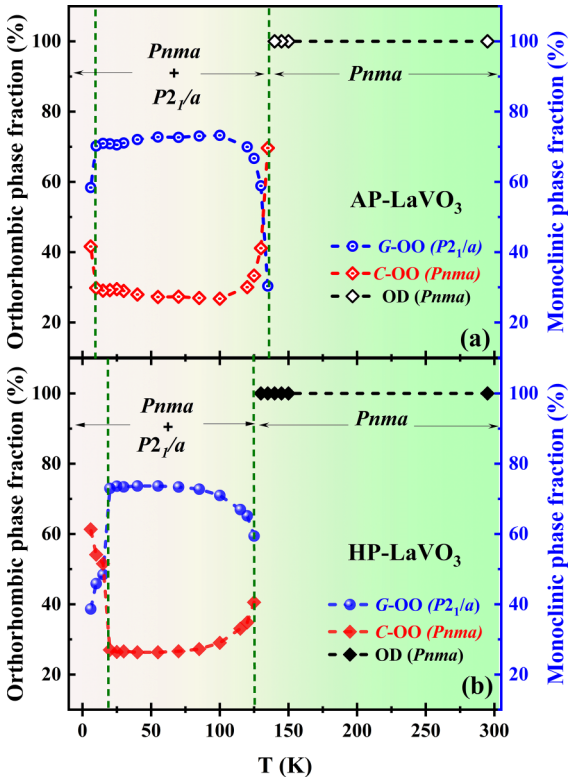

FIG. 9. Variation of phase fractions of orthorhombic and monoclinic phases of polycrystalline (a) AP-$LaVO_3$ and (b) HP-$LaVO_3$ as a function of temperature.

$T < T_{OO}^2$, *C*-OO begins to grow abruptly at the expense of *G*-OO, which is identified as the orbital flipping transition. This is manifested as an upturn in the magnetization data at low temperature, indicated by the blue arrow in Figs. 1(a) and 1(b). A recent report on neutron powder diffraction (NPD) studies on YVO_3 [10] explained the symmetry origin of Dzyaloshinskii-Moriya interaction (DMI) and its relation to the magnetization reversal phenomenon. The weak ferromagnetic component arising due to DMI acts opposite to the external magnetic field, due to which the magnetization measured in the low field cooled conditions is reduced. Thus, the generated weak ferromagnetic component in the sample can lower the magnetization overall to show magnetization reversal below T_{OO}^1. These observations indicate that the intensity of the weak ferromagnetic component opposing the applied magnetic field is directly related to the *G*-OO phase. It implies that the temperature dependence of magnetization corresponding to *G*- and *C*-OO results in the magnetization reversal in $LaVO_3$. For a detailed investigation of the magnitude of the weak ferromagnetic moment in the phase coexistence region, low-temperature NPD studies on ambient- and high-pressure synthesized $LaVO_3$ are needed.

Further, the entropy change across orbital ordering is investigated by recording temperature-dependent specific heat measurements on ambient- and high-pressure synthesized $LaVO_3$, as shown in Figs. 10(a) and 10(b), respectively. In AP-$LaVO_3$, a high-temperature anomaly was observed at ~135 K, related to orbital ordering and the antiferromagnetic ordering of vanadium atoms. This peak does not seem as sharp as that reported for single-crystal $LaVO_3$, where the anomalies corresponding to orbital and magnetic ordering can be distinctly seen [1,5]. Interestingly, HP-$LaVO_3$ shows two significant lambda-shaped anomalies, at ~125 K and ~20 K [shown in the inset of Fig. 10(b)]. The high-temperature anomaly corresponds to the orbital and the spin ordering of vanadium. The underlying orbital ordering concomitantly corresponds to the monoclinic (*G*-OO) and orthorhombic (*C*-OO) phases. The low-temperature anomaly corresponds to the orbital flipping transition from *G*- to *C*-OO phase. Further, the entropy change across orbital and spin ordering was analyzed by subtracting the lattice contribution for the specific heat.

Hence, the Debye-Einstein model is used to obtain the lattice contribution [45], and it is described as

$$C_{\text{ph}} = C_{\text{Debye}} + C_{\text{Einstein}} = \frac{9Ra_1}{x_D^3}\int_0^{x_D}\frac{x^4 e^x}{(e^x-1)^2}dx + 3R\sum_{n=1}^{2} b_n \frac{x_{E,n}^2 e^{x_{E,n}}}{(e^{x_{E,n}}-1)^2}.$$

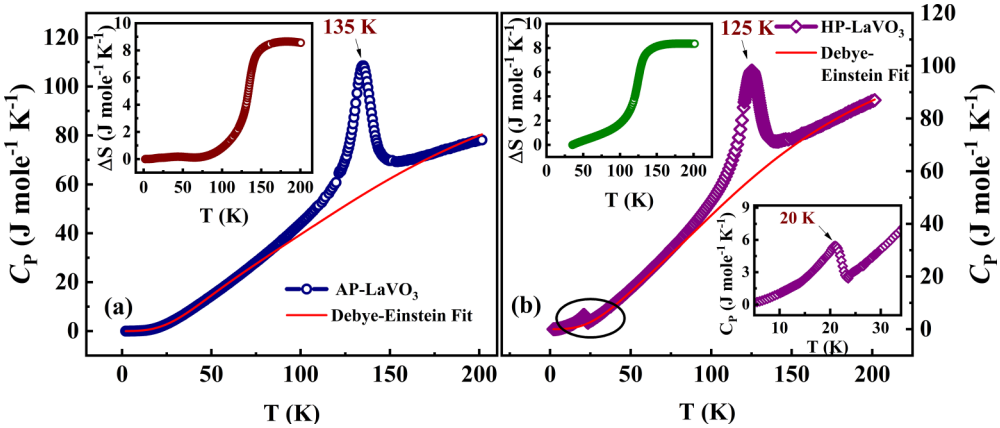

FIG. 10. Temperature-dependent specific heat measured for (a) AP-$LaVO_3$ and (b) HP-$LaVO_3$. Entropy change across T_{OO}^1 as a function of temperature is shown in the respective insets (left) in (a) and (b). Low-temperature orbital flipping transition at T_{OO}^2 in HP-$LaVO_3$ is shown in the right bottom inset of Fig. 10(b).

Here, R is the universal gas constant, and $x_{D,\,E} = \frac{\theta_{D,\,E}}{T}$, where $\theta_{D,\,E}$ are the Debye and Einstein temperatures, respectively. The sum of scale factors, a_n and b_n, corresponds to the total number of modes and is equivalent to the number of atoms per formula unit. One Debye and two Einstein terms were used to obtain a better fit to the curve. The coefficients a_1, b_1, and b_2 used for Debye and Einstein contributions are 1, 1, and 3, respectively. The fitting procedure yielded the following results: $\theta_D = 217(3)$ K, $\theta_{E1} = 271(7)$ K, and $\theta_{E2} = 626(2)$ K for AP-$LaVO_3$ and $\theta_D = 220(3)$ K, $\theta_{E1} = 278(1)$ K, and $\theta_{E2} = 541(3)$ K for HP-$LaVO_3$. The expected change in entropy due to magnetic ordering of V^{3+} ions with $S = 1$ is S_{mag} (at high T) $= R\ln(2S+1) = 9.13\,\mathrm{J\,mol^{-1}\,K^{-1}}$. In the case of $LaVO_3$, it is difficult to find the entropy change for magnetic ordering alone as orbital ordering occurs just 2 K away. The combined entropy change due to magnetic ordering as well as G- and C-OO at T_{OO}^1 is $\Delta S \sim 8.56$ and $8.35\,\mathrm{J\,mol^{-1}\,K^{-1}}$ for the ambient-pressure and high-pressure $LaVO_3$ phase, respectively, which is shown in the left inset of Figs. 10(a) and 10(b), respectively. This value is higher than the combined entropy change (for orbital and spin ordering) calculated for YVO_3, i.e., $\sim 2.55\,\mathrm{J\,mol^{-1}\,K^{-1}}$ [46]. The slight difference of the theoretical entropy change value from the entropy change obtained through the experiment could be due to the small entropy changes associated with the frustration of the spin or orbital ground state, as claimed by Khaliullin *et al.* [47]. The low-temperature G- to C-OO orbital flipping transition in HP-$LaVO_3$ yields an entropy change of $\Delta S \sim 1.45\,\mathrm{J\,mol^{-1}\,K^{-1}}$ and is comparable with YVO_3 for G-OO, i.e., $\Delta S \sim 1.74\,\mathrm{J\,mol^{-1}\,K^{-1}}$ [46].

The remarkable result of this study on orbital ordered states of $LaVO_3$ is the orbital flipping transition, where the orbital ordered phase changes from G- to C-OO. Some RVO_3 (R = Nd, Sm, Eu, Gd, Tb, and Y) show a gradual switching of the G- to the C-OO state with the coexistence of both phases down to low temperatures [4,6,10]. At 5 K, the phase fraction corresponding to C-OO for $NdVO_3 \sim 1\%$, $SmVO_3 \sim 25\%$, $EuVO_3 \sim 14\%$, $GdVO_3 \sim 70\%$, $TbVO_3 \sim 65\%$, and $YVO_3 \sim 96\%$. In addition, G- to C-OO flipping was observed in $TbVO_3$ with the application of external pressure, as reported by Zhou *et al.* [48]. Hence, the transformation from G- to C-OO is achieved either by chemical or external pressure [11,48]. It may be due to either the exchange striction mechanism or the change of orbital structure to minimize the superexchange interaction energy [49]. Also, pressure favors the C-OO ground state in smaller rare-earth oxides because of its smaller unit-cell volume [48]. Hence, due to the reduced unit-cell volume in HP-$LaVO_3$, the C-OO phase is favored over G-OO below T_{OO}^2. The orbital flipping transition can be shifted to higher temperatures if $LaVO_3$ is stabilized at higher pressure conditions. Stabilization of the C-OO state under high pressure is attributed to the covalency effect between rare earth d and V-3d orbitals, which increases as the unit cell volume reduces under pressure. High-pressure synthesis can be used as a tool to invoke C-OO in other RVO_3 perovskites.

IV. CONCLUSIONS

We have investigated the orbital states of $LaVO_3$ synthesized in ambient-pressure and high-pressure conditions using a high-angular-resolution synchrotron x-ray diffraction technique. The detailed structural analysis revealed that both compounds show slightly different oxygen stoichiometry and microstructure, which resulted in different magnetization reversal behavior. Further, both compounds show the coexistence of G- and C-OO states below T_{OO}^1 in $LaVO_3$. In addition, the orbital flipping transition from G- to C-OO is evidenced at low temperatures (T_{OO}^2). Our studies show that magnetization reversal in $LaVO_3$ correlates with the temperature evolution of coexisting magnetic phases corresponding to G- and C-OO states similar to other RVO_3 (R = Nd, Sm, Eu, Gd, Tb, and Y) perovskites.

ACKNOWLEDGMENTS

The authors would like to thank the Sheikh Saqr Laboratory and the International Centre for Materials Science at Jawaharlal Nehru Centre for Advanced Scientific Research for providing experimental facilities. A.S. acknowledges DST, SERB, and the government of India for the financial support. P.N.S acknowledges Jawaharlal Nehru Centre for Advanced Scientific Research for providing a research fellowship (JNC/S0484). Beamtime at CELLS-ALBA-synchrotron was granted through proposal 2020094682.

[1] L. D. Tung, M. R. Lees, G. Balakrishnan, and D. McK. Paul, Magnetization reversal in orthovanadate RVO_3 compounds (R = La, Nd, Sm, Gd, Er, and Y): Inhomogeneities caused by defects in the orbital sector of quasi-one-dimensional orbital systems, Phys. Rev. B **75**, 104404 (2007).

[2] S. Miyasaka, Y. Okimoto, M. Iwama, and Y. Tokura, Spin-orbital phase diagram of perovskite-type RVO_3 (R = rare-earth ion or Y), Phys. Rev. B **68**, 100406(R) (2003).

[3] H. Kawano, H. Yoshizawa, and Y. Ueda, Magnetic behavior of a mott-insulator YVO_3, J. Phys. Soc. Jpn. **63**, 2857 (1994).

[4] M. H. Sage, G. R. Blake, C. Marquina, and T. T. M. Palstra, Competing orbital ordering in RVO_3 compounds: High-resolution x-ray diffraction and thermal expansion, Phys. Rev. B **76**, 195102 (2007).

[5] Y. Ren, A. A. Nugroho, A. A. Menovsky, J. Strempfer, U. Rütt, F. Iga, T. Takabatake, and C. W. Kimball, Orbital-ordering-induced phase transition in $LaVO_3$ and $CeVO_3$, Phys. Rev. B **67**, 014107 (2003).

[6] M.-H. Sage, Orbital, charge and magnetic order of RVO_3 perovskites, Ph.D. thesis, University of Groningen, 2006.

[7] J. B. Goodenough, *Magnetism and the Chemical Bond* (Interscience, New York, 1963).

[8] J. Kanamori, Superexchange interaction and symmetry properties of electron orbitals, J. Phys. Chem. Solids **10**, 87 (1959).

[9] P. W. Anderson, Theory of magnetic exchange interactions: exchange in insulators and semiconductors, in *Solid State Physics*, edited by F. Seitz and D. Turnbull (Academic Press, 1963), Vol. 14, pp. 99–214.

[10] S. Sharma, P. N. Shanbhag, F. Orlandi, P. Manuel, S. Langridge, D. Adroja, M. K. Sanyal, and A. Sundaresan, Symmetry origin of the Dzyaloshinskii–Moriya interaction and magnetization reversal in YVO_3, Inorg. Chem. **60**, 2195 (2021).

[11] D. Bizen, K. Nakatsuka, T. Murata, H. Nakao, Y. Murakami, S. Miyasaka, and Y. Tokura, Orbital ordering in RVO_3 (R = Y, Tb) controlled by hydrostatic pressure, Phys. Rev. B **78**, 224104 (2008).

[12] S. Miyasaka, T. Yasue, J. Fujioka, Y. Yamasaki, Y. Okimoto, R. Kumai, T. Arima, and Y. Tokura, Magnetic field switching between the two orbital-ordered states in $DyVO_3$, Phys. Rev. Lett. **99**, 217201 (2007).

[13] H. C. Nguyen and J. B. Goodenough, Magnetic studies of some orthovanadates, Phys. Rev. B **52**, 324 (1995).

[14] Y. Ren, T. T. M. Palstra, D. I. Khomskii, E. Pellegrin, A. A. Nugroho, A. A. Menovsky, and G. A. Sawatzky, Temperature-induced magnetization reversal in a YVO_3 single crystal, Nature (London) **396**, 441 (1998).

[15] Y. Ren, T. T. M. Palstra, D. I. Khomskii, A. A. Nugroho, A. A. Menovsky, and G. A. Sawatzky, Magnetic properties of YVO_3 single crystals, Phys. Rev. B **62**, 6577 (2000).

[16] Y. Kimishima, Y. Ichiyanagi, K. Shimizu, and T. Mizuno, N-type ferrimagnetism of $SmVO_3$, J. Magn. Magn. Mater. **210**, 244 (2000).

[17] Y. Kimishima, M. Uehara, and T. Saitoh, Ca-doping effects on N-type ferrimagnetism of $NdVO_3$, Solid State Commun. **133**, 559 (2005).

[18] R. Saha, F. Fauth, V. Caignaert, and A. Sundaresan, Coexistence of G- and C-type orbital ordered phases and its correlation with magnetization reversal in YVO_3, Phys. Rev. B **95**, 184107 (2017).

[19] B. Roberge, S. Jandl, A. A. Nugroho, T. T. Palstra, L. D. Tung, and G. Balakrishnan, Study of phase coexistence in YVO_3 and $LaVO_3$, J. Raman Spectrosc. **46**, 1157 (2015).

[20] P. N. Shanbhag, Structural & magnetic investigations of corundum & perovskite structures of the compound AMO_3, M.S. thesis, Jawaharlal Nehru Centre for Advanced Scientific Research, Bengaluru, India, 2017.

[21] F. Fauth, I. Peral, C. Popescu, and M. Knapp, The new material science powder diffraction beamline at ALBA synchrotron, Powder Diff. **28**, S360 (2013).

[22] F. Fauth, R. Boer, F. Gil-Ortiz, C. Popescu, O. Vallcorba, I. Peral, D. Fullà, J. Benach, and J. Juanhuix, The crystallography stations at the Alba synchrotron, Eur. Phys. J. Plus **130**, 1 (2015).

[23] P. J. Van Der Linden *et al.*, A compact and versatile dynamic flow cryostat for photon science, Rev. Sci. Instrum. **87**, 115103 (2016).

[24] N. S. N. Shirakawa and M. I. M. Ishikawa, Anomalous diamagnetism of a perovskite $LaVO_3$, Jpn. J. Appl. Phys. **30**, L755 (1991).

[25] A. V. Mahajan, D. C. Johnston, D. R. Torgeson, and F. Borsa, Magnetic properties of $LaVO_3$, Phys. Rev. B **46**, 10966 (1992).

[26] See Supplemental Material at http://link.aps.org/supplemental/10.1103/PhysRevB.108.134115 for temperature-dependent DC magnetization measurements at different magnetic fields, the Curie-Weiss fit, XPS spectra, the room-temperature synchrotron x-ray diffraction profile, and the W-H plot obtained for AP- and HP- $LaVO_3$ compounds.

[27] P. Sepiedeh, Crystallinity, magnetic and electrical properties of Bi doped $LaVO_3$, M.Sc. thesis, Brock University, 2012.

[28] S. J. Gharetape, M. P. Singh, F. S. Razavi, D. A. Crandles, L. Y. Zhao, and K. T. Leung, Effect of vanadium deficiency on properties of polycrystalline $LaVO_3$, Appl. Phys. Lett. **98**, 052509 (2011).

[29] T. Sakai, G. Y. Adachi, J. Shiokawa, and T. Shin-ike, Magnetic properties of rare-earth vanadites $LnVO_3$, J. Appl. Phys. **48**, 379 (1977).

[30] J.-Q. Yan, J.-S. Zhou, and J. B. Goodenough, Unusually strong orbit-lattice interactions in the RVO_3 perovskites, Phys. Rev. Lett. **93**, 235901 (2004).

[31] J.-S. Zhou, Y. Ren, J.-Q. Yan, J. F. Mitchell, and J. B. Goodenough, Frustrated superexchange interaction versus orbital order in a $LaVO_3$ crystal, Phys. Rev. Lett. **100**, 046401 (2008).

[32] A. Muñoz, J. Alonso, M. Casais, M. Martínez-Lope, J. Martínez, and M. Fernández-Díaz, Thermal evolution of the crystallographic and magnetic structure in $LuVO_3$: A neutron diffraction study, Chem. Mater. **16**, 1544 (2004).

[33] M. Corti, F. Cintolesi, A. Lascialfari, A. Rigamonti, and G. Rossetti, Magnetic properties of YVO_3 from susceptibility and 89Y NMR measurements, J. Appl. Phys. **81**, 5286 (1997).

[34] X. Liu *et al.*, In situ modulation of a-site vacancies in $LaMnO_{3.15}$ perovskite for surface lattice oxygen activation and boosted redox reactions, Angew. Chem. Int. Ed. **60**, 26747 (2021).

[35] A. Jana, S. Karwal, R. Choudhary, and D. Phase, Studies of electronic and magnetic properties of $LaVO_3$ thin film, in *DAE Solid State Physics Symposium 2017*, AIP Conf. Proc. No. 1942 (AIP, New York, 2018), p. 080016.

[36] E. Beyreuther, S. Grafström, L. M. Eng, C. Thiele, and K. Dörr, XPS investigation of Mn valence in lanthanum manganite thin films under variation of oxygen content, Phys. Rev. B **73**, 155425 (2006).

[37] P. Bordet, C. Chaillout, M. Marezio, Q. Huang, A. Santoro, S. W. Cheong, H. Takagi, C. S. Oglesby, and B. Batlogg, Structural aspects of the crystallographic-magnetic transition in $LaVO_3$ around 140 K, J. Solid State Chem. **106**, 253 (1993).

[38] G. Williamson and W. Hall, X-ray line broadening from filed aluminium and wolfram, Acta Metall. **1**, 22 (1953).

[39] P. N. Shanbhag, A. Joseph, F. Orlandi, P. Manuel, R. Mahendiran, F. Fauth, C. Narayana, A. Sundaresan, and C. N. R. Rao, Effects of Ga doping on the phase transitions of V_2O_3, Phys. Rev. B **105**, 064103 (2022).

[40] H. Rotella, U. Lüders, P.-E. Janolin, V. H. Dao, D. Chateigner, R. Feyerherm, E. Dudzik, and W. Prellier, Octahedral tilting in strained $LaVO_3$ thin films, Phys. Rev. B **85**, 184101 (2012).

[41] M. H. Sage, G. R. Blake, G. J. Nieuwenhuys, and T. T. M. Palstra, Evidence for electronic phase separation between orbital orderings in $SmVO_3$, Phys. Rev. Lett. **96**, 036401 (2006).

[42] M. Martínez-Lope, J. Alonso, M. Retuerto, M. Fernández-Díaz, M. J. Martínez-Lope, J. A. Alonso, M. Retuerto, and M. T. Fernández-Díaz, Evolution of the crystal structure of RVO_3 (R = La, Ce, Pr, Nd, Tb, Ho, Er, Tm, Yb, Lu, Y) perovskites from neutron powder diffraction data, Inorg. Chem. **47**, 2634 (2008).

[43] I. Loa, X. Wang, K. Syassen, H. Roth, T. Lorenz, M. Hanfland, and Y.-L. Mathis, Crystal structure and the Mott–Hubbard gap

in $YTiO_3$ at high pressure, J. Phys. Condens. Matter **19**, 406223 (2007).

[44] J. Alonso, M. Martinez-Lope, M. Casais, and M. Fernandez-Diaz, Evolution of the Jahn-Teller distortion of MnO_6 octahedra in $RMnO_3$ perovskites (R = Pr, Nd, Dy, Tb, Ho, Er, Y): A neutron diffraction study, Inorg. Chem. **39**, 917 (2000).

[45] S. Ghara, N. V. Ter-Oganessian, and A. Sundaresan, Linear magnetoelectric effect as a signature of long-range collinear antiferromagnetic ordering in the frustrated spinel $CoAl_2O_4$, Phys. Rev. B **95**, 094404 (2017).

[46] G. R. Blake, T. T. M. Palstra, Y. Ren, A. A. Nugroho, and A. A. Menovsky, Neutron diffraction, x-ray diffraction, and specific heat studies of orbital ordering in YVO_3, Phys. Rev. B **65**, 174112 (2002).

[47] G. Khaliullin, P. Horsch, and A. M. Oleś, Spin order due to orbital fluctuations: Cubic vanadates, Phys. Rev. Lett. **86**, 3879 (2001).

[48] J.-S. Zhou, J. B. Goodenough, J.-Q. Yan, and Y. Ren, Superexchange interaction in orbitally fluctuating RVO_3, Phys. Rev. Lett. **99**, 156401 (2007).

[49] I. Solovyev, Modeling of complex oxide materials from the first principles: Systematic applications to vanadates RVO_3 with distorted perovskite structure, J. Comput. Electron. **10**, 21 (2011).